J Mater Sci (2018) 53:6494–6504

Chemical routes to materials

Electrostatic self-assembly behaviour of exfoliated $Sr_2Nb_3O_{10}^-$ nanosheets and cobalt porphyrins: exploration of non-noble electro-catalysts towards hydrazine hydrate oxidation

Binbin Pan[1], Jiasheng Xu[1], Xiaobo Zhang[1], Jinpeng Li[1], Mengjun Wang[1], Juanjuan Ma[1], Lin Liu[1], Dongen Zhang[1], and Zhiwei Tong[1,2,3,*]

[1] School of Chemical Engineering, Huaihai Institute of Technology, Lianyungang 222005, China
[2] College of Chemistry and Chemical Engineering, Lanzhou University, Lanzhou 730000, China
[3] SORST, Japan Science and Technology Agency (JST), Kawaguchi Center Building 4-1-8, Kawaguchi-shi, Saitama 332-0012, Japan

Received: 11 August 2017
Accepted: 12 January 2018
Published online: 22 January 2018

ABSTRACT

In our research, a convenient exfoliation/restacking route was used to fabricate a sandwich-structured nanocomposite of $Sr_2Nb_3O_{10}$/CoTMPyP [5,10,15,20-tetrakis(*N*-methylpyridinium-4-yl)porphyrinato cobalt] via electrostatic interaction between colloidal dispersion and cobalt porphyrin aqueous solution. The final self-assembled products were characterized by XRD, FTIR, UV–Vis, SEM, TEM, AFM, and ICP. During the exfoliation procedure, the well-dispersed $Sr_2Nb_3O_{10}^-$ colloidal dispersion was obtained with the zeta potential value of − 44.2 mV. Additionally, the existence of unilamellar $Sr_2Nb_3O_{10}^-$ nanosheet was evidenced by AFM, and zeta potential values of the reassembly process with the addition of CoTMPyP aqueous solution into the colloidal dispersion were measured by a Zetasizer Nano apparatus. Above all, the final $Sr_2Nb_3O_{10}$/CoTMPyP hybrid film displayed excellent electro-catalytic activities towards hydrazine hydrate oxidation with peak potential at 0.158 V in pH 7.0 PBS indicated by CV measurements; moreover, a detection limit of 3.52×10^{-5} M was obtained in the concentration range of 5×10^{-5}–9.9×10^{-4} M at a signal-to-noise ratio of 3.0.

Introduction

Hydrazine hydrate was not only widely applied as a strong reducing agent, pharmaceutical intermediates, antioxidants, etc., but also considered as a type of fuel cell with high energy density, except for methanol, formic acid fuel cell [1–4]. Comparing with the efficient oxidation of methanol and formic acid limited to noble metal electro-catalysts only, the possible electro-catalytic oxidation of hydrazine hydrate on non-noble metal electrodes became the advantage of direct hydrazine fuel cell. Therefore, much attention

Address correspondence to E-mail: zhiweitong575@hotmail.com

https://doi.org/10.1007/s10853-018-2033-x

was focused on the exploration of efficient non-noble electro-catalysts towards hydrazine hydrate oxidation [5–10]. It is worth mentioning that a well-known class of naturally occurring compounds in biological systems, porphyrins and their derivatives played an important role in the development of electro-catalysts for different reactions because of the intriguing redox properties [11]; in particular, transition metal porphyrins complexes were reported to exhibit excellent catalytic activity towards hydrazine hydrate oxidation [8]. To overcome the own limitations, or even to improve their properties, metalloporphyrin complexes have been usually immobilized into the rigid inorganic matrix [12, 13]. However, the tedious and time-resuming work-up was required for introducing functional guest spices in large volume into the interlayer by virtue of the traditional ion-exchange process; consequently, the convenient and effective route for fabricating functional hybrids was urgent to be developed.

On the other hand, two-dimensional layered metal oxide semiconductors (LMOSs) nanosheets derived from the parent layered materials have gained popularity in fundamental research [14–18] since the production of graphene with amazing functionalities. Consequently, an interesting osmotic swelling/exfoliation route was advanced for producing unilamellar LMOSs nanosheet in high quality through the permeation of bulky tetraalkylammonium cations (TAA^+) and large amounts of H_2O molecules into the interlayer region to greatly weaken the interactions between neighbouring sheets [19, 20]. Owing to the structural diversity and extraordinary electronic properties, the obtained nanosheets with atomic or molecular thickness and micrometer-order lateral sizes were thus exploited for application in electronic, magnetic, optical, electrochemical, and catalytic nanodevices [17]; more interestingly, the negatively charged nanosheets can serve as promising building blocks for the construction of functional hybrid materials [21]. At present, the hybridization of a broad spectrum of guest species including transition metal complex [22, 23], transition metal nanoparticles [24, 25], and LDHs nanosheets [26, 27] with exfoliated LMOSs nanosheets have been achieved through electrostatic self-assembly reaction; nevertheless, the introduction of bulky organic functional pigments into the interlayer of LMOSs using the exfoliation/restacking method remained less studied [28].

As we all know, Dion–Jacobson (D–J)-type layered perovskites were highly favoured among two-dimensional LMOSs, one representative example of which was $KSr_2Nb_3O_{10}$ characteristic of triple-octahedral arrangements along the host layer (schematic illustration of the structure is in Fig. 1) [29], and the protonated product can be also dispersed in the TAAOH aqueous solution to form unilamellar nanosheet maintaining excellent properties of semiconductor from the parent [30]; herein, the promising inorganic matrix of $KSr_2Nb_3O_{10}$ was selected as the starting material, and $Sr_2Nb_3O_{10}^-$ nanosheets were obtained by dispersing the protonated product into TBAOH [$(C_4H_9)_4NOH$] aqueous solution; what is more, the final $Sr_2Nb_3O_{10}$/CoTMPyP nanocomposites were fabricated via electrostatic interaction between $Sr_2Nb_3O_{10}^-$ nanosheets colloidal dispersion and cobalt porphyrin aqueous solution (Fig. 2), and electro-catalytic measurements towards hydrazine hydrate oxidation adopting the $Sr_2Nb_3O_{10}$/CoTMPyP assembled hybrid film were taken.

Experimental

Preparation of $Sr_2Nb_3O_{10}$/CoTMPyP nanocomposite

The host material of $KSr_2Nb_3O_{10}$ was synthesized through a conventional solid-state reaction referring to a previously reported literature [31]. The obtained product (1 g) was then converted into the protonic

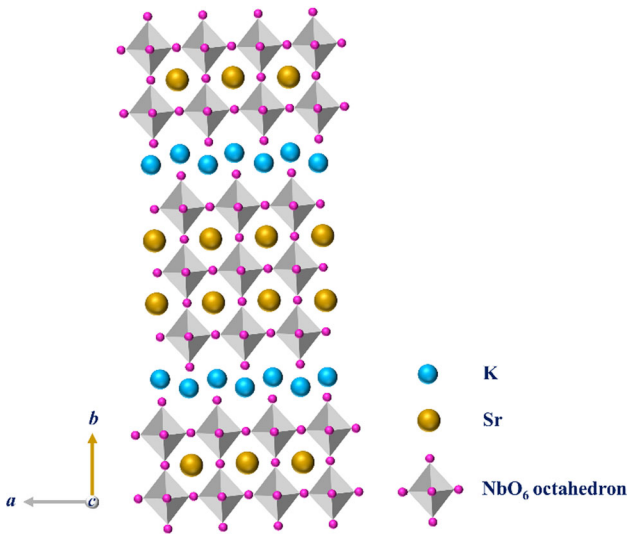

Figure 1 Schematic illustration of $KSr_2Nb_3O_{10}$ structure.

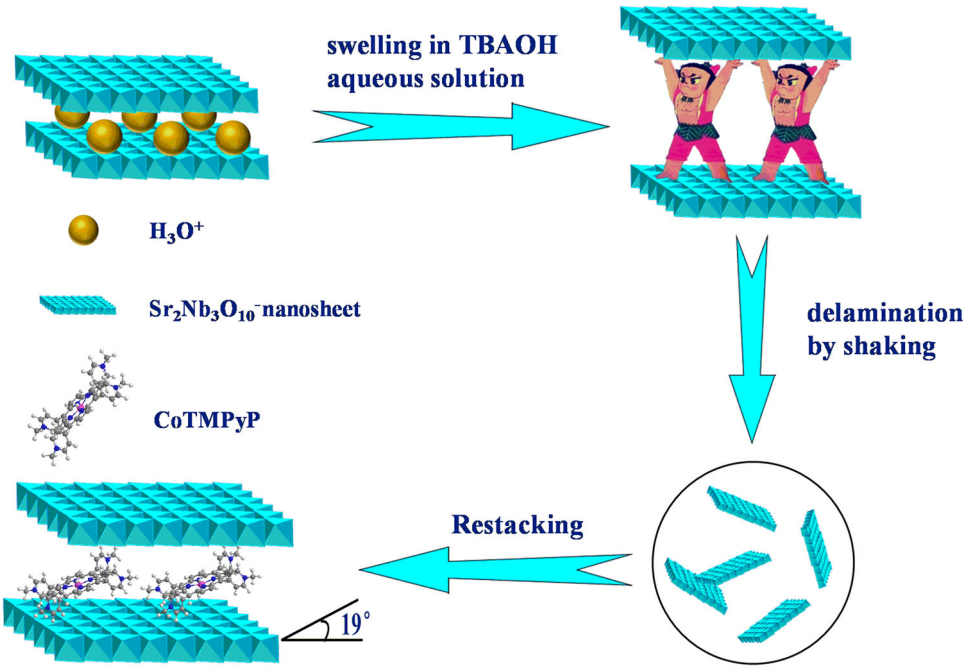

Figure 2 Schematic illustration of the reassembly process between $Sr_2Nb_3O_{10}^-$ nanosheets and cobalt porphyrins.

form of $HSr_2Nb_3O_{10}$ in 6 M HNO_3 (30 ml) for three times (24 h/per time). Concerning the preparation of exfoliated $Sr_2Nb_3O_{10}^-$ nanosheets, it was realized by dispersing the acidified product into stoichiometric amounts of 10 (wt)% TBAOH aqueous solution with uniform agitation for 5 days (the molar ratio of $TBA^+/H^+ = 1$ was adopted), and the final translucent colloidal suspension was centrifuged at 3000 rpm for 10 min to remove the unexfoliated particles. In order to fabricate the $Sr_2Nb_3O_{10}$/CoTMPyP nanocomposite, 1 mM CoTMPyP aqueous solution (2, 3, 4 ml) was separately added into the obtained $Sr_2Nb_3O_{10}^-$ nanosheets colloidal dispersion above (4, 3, 2 ml), and then the flocculated precipitates were washed with distilled water and anhydrous ethanol repeatedly and dried at 50 °C in a vacuum oven for 24 h. The final nanocomposites were labelled as $Sr_2Nb_3O_{10}$/$CoTMPyP_{0.5}$, $Sr_2Nb_3O_{10}$/$CoTMPyP_1$, $Sr_2Nb_3O_{10}$/$CoTMPyP_2$, according to the corresponding volume ratio of CoTMPyP aqueous solution and the colloidal dispersion (CoTMPyP/$Sr_2Nb_3O_{10}^-$ = 0.5, 1, 2).

Characterization

Shimadzu FTIR-8400S spectrometer was employed for collecting infrared spectra of the products with the use of KBr pellets. UV–Vis absorption spectra were recorded with a UV–Vis spectrometer (UV-2550). A RINT 2000 diffractometer (Cu Kα radiation, $\lambda = 0.154$ nm, Rigaku) was used to obtain X-ray diffraction patterns of the samples with 2θ going from 2° to 40°. The scanning electron microscopic images of the samples were acquired by a JSM-5600 apparatus (JEOL), atomic force microscope (AFM) images were taken with a Bruker dimension edge SPM apparatus adopting the peak force tapping mode, and high-resolution transmission electron microscope (HRTEM) images were taken with the apparatus (JEOL, JEM-2010); the specimens were prepared by sonicating the products in ethanol for 10 min in advance and evaporating a drop of the resulting suspension onto a copper grid. Zeta potential was measured by a Malvern Zetasizer Nano instrument, and water at 25 °C was selected as the dispersion solvent. The concentration of Co element in the final hybrid solution was analysed by an inductively coupled plasma (ICP) spectrometer (CAP6300).

Electrochemical measurements

Electrochemical measurements were performed in a conventional three-electrode cell using a CHI660c electrochemical workstation, platinum wire electrode and a saturated calomel electrode (SCE) were used as

the auxiliary electrode and the reference electrode, respectively, and the $Sr_2Nb_3O_{10}$/$CoTMPyP_1$ hybrid thin-film modified glass carbon electrode (GCE) was used as the working electrode by coating 7.5 μl 1 mg/ml $Sr_2Nb_3O_{10}$/$CoTMPyP_1$ aqueous dispersion on GCE and dried naturally for 24 h. With the purpose of investigating electro-catalytic properties of the final hybrid film towards hydrazine hydrate oxidation, the measuring techniques of cyclic voltammetry (CV) and differential pulse voltammetry (DPV) were adopted in this experiment. All buffer solutions including Britton–Robinson (B–R) buffer solution and phosphate buffer solution (PBS) in the electrochemical measurements were purged with nitrogen for 20 min prior to the experiments.

Results and discussion

XRD analysis

The sintered product of $KSr_2Nb_3O_{10}$ was identified by X-ray diffraction analysis in Fig. 3, the basal spacing (d_{002}) of the starting material was calculated as 1.46 nm on the basis of the angle (6.03°) of (002) diffraction peak, and the formation of H_3O^+ in the interlayer led the basal spacing of the acidified product an increase by 1.62 nm; upon the reassembly of $Sr_2Nb_3O_{10}^-$ nanosheets and CoTMPyP cations, the (002) diffraction peaks of the three obtained nanocomposites shifted towards almost the same lower 2θ angle of ~ 4.3°, indicating that the basal spacings of $Sr_2Nb_3O_{10}$/CoTMPyP hybrids increased to ~ 2.05 nm, correspondingly. As observed in Fig. 3c, the XRD pattern of $Sr_2Nb_3O_{10}^-$ nanosheets colloidal suspension, the disappearance of sharp peaks suggested the collapse of layered structure [32, 33]. On the other hand, the arrangement model of the $Sr_2Nb_3O_{10}$/$CoTMPyP_1$ hybrid can be postulated by the inclined angle of CoTMPyP molecules in the galley. According to the interlayer distance of the $Sr_2Nb_3O_{10}$/$CoTMPyP_1$ hybrid (the value was calculated as 0.59 nm by subtracting the $Sr_2Nb_3O_{10}^-$ layer thickness of 1.44 nm) [16] and the CoTMPyP molecular dimension (18 × 18 Å, estimated by MM2 calculation), it was concluded that CoTMPyP molecules were located in the galley of the $Sr_2Nb_3O_{10}$/$CoTMPyP_1$ hybrid by an inclined angle of 19° to form a monolayer in Fig. 2.

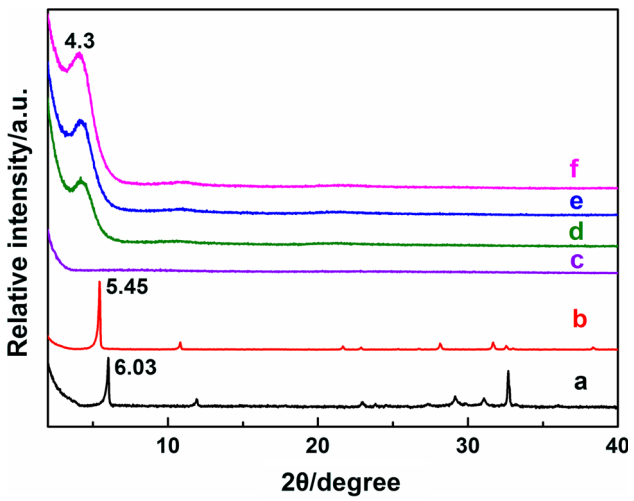

Figure 3 XRD patterns of (*a*) $KSr_2Nb_3O_{10}$, (*b*) $HSr_2Nb_3O_{10}$, (*c*) $Sr_2Nb_3O_{10}^-$ and (*d*) $Sr_2Nb_3O_{10}$/$CoTMPyP_{0.5}$, (*e*) $Sr_2Nb_3O_{10}$/$CoTMPyP_1$, (*f*) $Sr_2Nb_3O_{10}$/$CoTMPyP_2$.

Zeta potential analysis

As can be seen from Fig. 4a, it presented the photograph of the reassembly process between $Sr_2Nb_3O_{10}^-$ nanosheets colloidal suspension and CoTMPyP aqueous solution, the dark red flocculent precipitates appear at once as soon as CoTMPyP aqueous solution was added into $Sr_2Nb_3O_{10}^-$ nanosheets colloidal dispersion, and the generation of the flocculent precipitates (i.e. the $Sr_2Nb_3O_{10}$/CoTMPyP nanocomposite) can be illustrated as the electrostatic interaction between $Sr_2Nb_3O_{10}^-$ nanosheets with negative charge and cobalt porphyrin cations. Furthermore, the reassembly process can be finished within 20 min, and this is the advantage of exfoliation/restacking route over the traditional ion-exchange method.

Tyndall light scattering phenomenon of the $Sr_2Nb_3O_{10}^-$ colloidal dispersion is exhibited in Fig. 4b, suggesting the occurrence of exfoliation to a certain degree [34]; in order to further investigate the delamination/restacking process, the measurement of the surface potential was made by a Zetasizer Nano instrument. The zeta potential value of $Sr_2Nb_3O_{10}^-$ nanosheets colloidal dispersion was − 44.2 mV in the light of the zeta potential report in Figure S3; regarding the formation of $Sr_2Nb_3O_{10}^-$ nanosheets, it can be explained as the penetration of TBA^+ ions in large volume into the interlayer of the acidified product, and expansion of the interlayer spacing to greatly weaken the interactions of neighbouring nanosheets [20]. Additionally, the influence

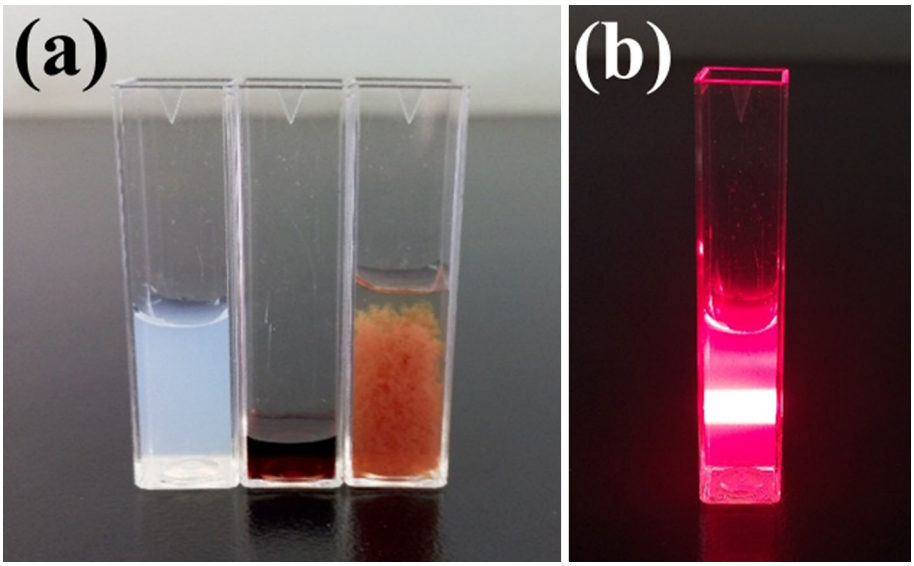

Figure 4 **a** Photographs of $Sr_2Nb_3O_{10}^-$ nanosheets colloidal suspension (left), CoTMPyP aqueous solution (middle), and the mixture of $Sr_2Nb_3O_{10}^-$ nanosheets colloidal suspension and CoTMPyP aqueous solution (right). **b** Tyndall phenomenon of $Sr_2Nb_3O_{10}^-$ nanosheets colloidal dispersion.

of the volume ratio between CoTMPyP aqueous solution and $Sr_2Nb_3O_{10}^-$ nanosheets colloidal suspension on the zeta potential values was investigated; it can be observed that as the increase in CoTMPyP aqueous solution volume added into $Sr_2Nb_3O_{10}^-$ nanosheets colloidal dispersion, the zeta potential values increased gradually (Fig. 5) and the pH values decreased from 12.21 to 6.55. The zeta potential absolute value was approximately zero at the volume ratio of 0.22, and the zeta potential value change in the reassembly process also provides the support for the occurrence of flocculation phenomenon between $Sr_2Nb_3O_{10}^-$ nanosheets colloidal dispersion and CoTMPyP aqueous solution.

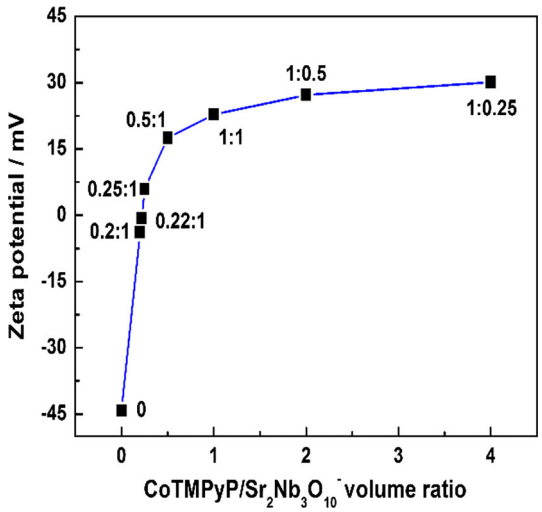

Figure 5 Relationship curve between zeta potential values and CoTMPyP/$Sr_2Nb_3O_{10}^-$ volume ratios.

IR spectra analysis

The successful introduction of CoTMPyP molecules into the galley of $Sr_2Nb_3O_{10}^-$ laminate can also be identified by IR spectra analysis (Figure S1). The absorption peaks of $KSr_2Nb_3O_{10}$ host material were mainly in the range of 1000–400 cm^{-1} (Nb–O stretching vibration); furthermore, the IR spectra of CoTMPyP molecules exhibited typical characteristic peaks such as 1640 cm^{-1}, and 1560, 1459, 1401 cm^{-1}, which were assigned to C=N stretching vibration in the pyridine substituent, and C=N, C=C stretching vibration in the porphyrin rings, respectively. Similarly, several absorption bands (1638, 1400, 1121, 924, and 582 cm^{-1}) were observed in the IR spectra of the $Sr_2Nb_3O_{10}$/$CoTMPyP_1$ nanocomposite, illustrating that the final hybrid contains not only the $Sr_2Nb_3O_{10}^-$ host laminate, but also CoTMPyP molecules. Furthermore, the interaction between guest molecules and host materials caused a slight shift in the characteristic peaks for $Sr_2Nb_3O_{10}$/CoTMPyP compared with IR spectrum of pure CoTMPyP [35].

UV–visible absorption spectra analysis

As shown in Figure S2, typically, the Soret band and Q band of CoTMPyP aqueous solution appeared at 437 and 549 nm, respectively; however, the self-assembly reaction of $Sr_2Nb_3O_{10}^-$ nanosheets and CoTMPyP cations led to red shifts in the Soret bands and Q bands of the obtained dark-brown hybrid

films; in detail, $Sr_2Nb_3O_{10}$/CoTMPyP$_{0.5}$, $Sr_2Nb_3O_{10}$/CoTMPyP$_1$, $Sr_2Nb_3O_{10}$/CoTMPyP$_2$ hybrids exhibited 8-, 9-, 10-nm red shifts in the Soret bands, and 1-, 2-, 3-nm red shifts in Q bands, respectively, demonstrating the intense interaction between $Sr_2Nb_3O_{10}^-$ laminate and CoTMPyP cations [36]. Additionally, owing to the different intermolecular interactions of stacked metalloporphyrin molecules, the occurrence of a broadening phenomenon was in the absorption spectra of the final reassembly products when compared to free CoTMPyP absorption bands, which was coincident with several previous reports [13, 37, 38].

Morphology analysis

The surface morphology of $KSr_2Nb_3O_{10}$, $HSr_2Nb_3O_{10}$, and the reassembly product, $Sr_2Nb_3O_{10}$/CoTMPyP$_1$, was acquired by SEM and TEM as shown in Fig. 6, comparing with that of the origin material, $KSr_2Nb_3O_{10}$, the smooth surface of the acidified product indicated higher crystallinity corresponding to XRD data of the acidified product, and the particle size of the protonated product ranges from 0.1 to ca. 10 μm. In order to confirm the existence of $Sr_2Nb_3O_{10}^-$ nanosheets in the delamination process, the obtained colloidal dispersion was characterized by AFM adopting a peak force tapping mode. As can be seen clearly from Fig. 7a, there existed several nanosheets in irregular shape dispersing on the mica substrate, which provides strong evidence for the occurrence of exfoliation. On the side, the appearance of few stacked nanosheets reflected the randomness in the delamination process as well. On the basis of the height profile along the marked white line, the thickness of $Sr_2Nb_3O_{10}^-$ nanosheet was measured as ca. 2.18 nm, and the additional thickness over the crystallographic thickness of the $Sr_2Nb_3O_{10}^-$ laminate (1.44 nm) should be attributed to water molecules and counterions (TBA^+) absorbed on the surface of the nanosheet [39–41], suggesting the production of unilamellar $Sr_2Nb_3O_{10}^-$ nanosheet.

After the self-assembly of $Sr_2Nb_3O_{10}^-$ nanosheets and CoTMPyP molecules, the overall crystallinity of the final hybrid has decreased; nevertheless, sandwich-structure $Sr_2Nb_3O_{10}$/CoTMPyP$_1$ nanocomposite was constructed via electrostatic interaction between $Sr_2Nb_3O_{10}^-$ nanosheets and cobalt porphyrin cations (Fig. 6c, d). As labelled in the partial enlarged drawing (Fig. 6e), the thickness was approximately 4.08 nm with double basal spacings; namely the basal spacing of $Sr_2Nb_3O_{10}$/CoTMPyP$_1$ nanocomposite was ca. 2.04 nm, which corresponds well with XRD data (2.05 nm) [42–45]. Furthermore, the morphology of $Sr_2Nb_3O_{10}$/CoTMPyP$_1$ nanocomposite was also analysed by AFM shown in Fig. 7b, and exfoliated $Sr_2Nb_3O_{10}^-$ nanosheets in the delamination process didn't disturb the reconstruction of the lamellar structure of the final hybrid. The final hybrid consisted of several stacked nanoplates, and the basal spacing of $Sr_2Nb_3O_{10}$/CoTMPyP$_1$ was measured as ca. 2.0 and 2.26 nm according to the height profile along the marked white line, which was in good agreement with XRD data (2.05 nm). Besides, the quantitative analysis of the final hybrid was conducted using an ICP instrument, and 2.4 μmol Co element in per litre $Sr_2Nb_3O_{10}$/CoTMPyP$_1$ nanocomposite solution was detected.

Electrochemical characterization

Figure 8 gives CV curves of CoTMPyP aqueous solution, $Sr_2Nb_3O_{10}$/CoTMPyP$_1$ hybrid film, and $KSr_2Nb_3O_{10}$ modified GCE in pH 12.0 B–R buffer solution at the scan rate of 100 mV s^{-1}. Owing to the sensitivity of metalloporphyrin molecules to pH conditions, undefined oxidation/reduction peaks were present in CV curves of CoTMPyP aqueous solution; on the contrary, the assembled hybrid film displayed two pairs of similar well-defined oxidation/reduction peaks, with the redox potentials of one couple of the oxidation/reduction peaks (I_{a1}, I_{c1}) at − 0.709 and − 0.754 V, and the redox potentials of the other couple of oxidation/reduction peaks (I_{a2}, I_{c2}) at − 0.853 and − 0.959 V, corresponding to $Co^{III/II}$TMPyP and $Co^{II/I}$TMPyP redox couple, respectively [46]. The reversible redox process can be illustrated by the following expressions: $Co^{II}TMPyP^{4+} + e^- \rightarrow Co^{I}TMPyP^{3+}$ (peak I_{c2}), $Co^{I}TMPyP^{3+} - e^- \rightarrow Co^{II}TMPyP^{4+}$ (peak I_{a2}), $Co^{III}TMPyP^{5+} + e^- \rightarrow Co^{II}TMPyP^{4+}$ (peak I_{c1}), $Co^{II}TMPyP^{4+} - e^- \rightarrow Co^{III}TMPyP^{5+}$ (peak I_{a1}). The presence of well-defined oxidation/reduction peaks and the increase in the peak current intensity in the final hybrid film revealed that the immobilization of CoTMPyP molecules on the support matrix of $Sr_2Nb_3O_{10}^-$ was an effective method for utilizing excellent electrochemical performance of metalloporphyrin in harsh conditions.

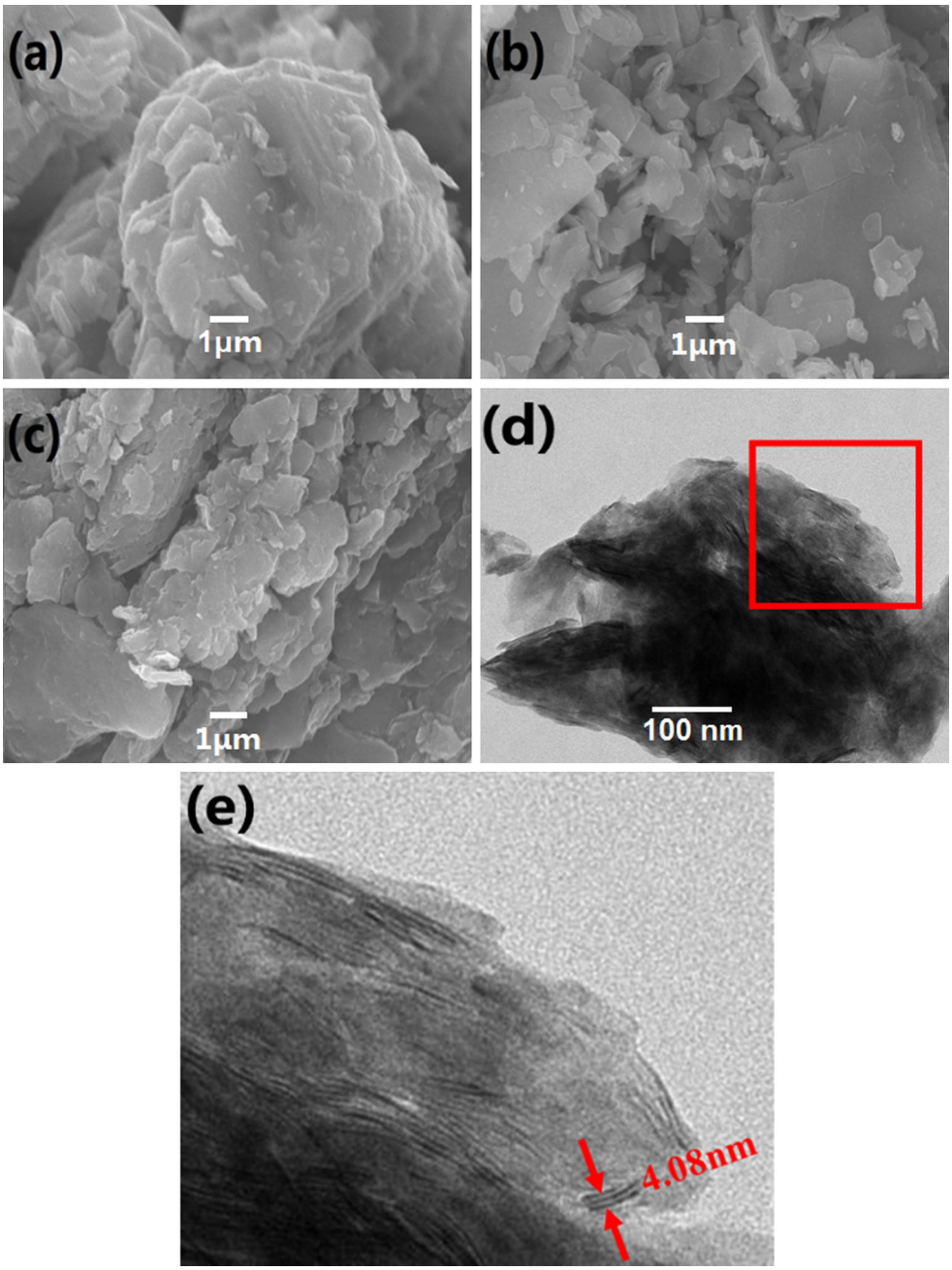

Figure 6 SEM images of **a** $KSr_2Nb_3O_{10}$, **b** $HSr_2Nb_3O_{10}$ and **c** $Sr_2Nb_3O_{10}$/$CoTMPyP_1$, TEM image of **d** $Sr_2Nb_3O_{10}$/$CoTMPyP_1$ and **e** the partial enlarged drawing of the rectangle in **d**.

Electro-catalytic properties of $Sr_2Nb_3O_{10}$/CoTMPyP hybrid film towards hydrazine hydrate oxidation

The electrochemical oxidation of $N_2H_4{\cdot}H_2O$ using $Sr_2Nb_3O_{10}$/$CoTMPyP_1$ modified GCE was attempted in 0.2 M pH 7.0 PBS, and a comparison of $KSr_2Nb_3O_{10}$/GCE, $Sr_2Nb_3O_{10}$/$CoTMPyP_1$ modified GCE and bare GC at 100 mV s^{-1} was made (Fig. 9A). Concerning the electro-catalytic oxidation effect of bare GC and the host material modified GCE, they barely work in the $N_2H_4{\cdot}H_2O$ oxidation process, while the oxidation potential of $Sr_2Nb_3O_{10}$/$CoTMPyP_1$ modified GCE appeared at 0.158 V, suggesting that the obtained assembled hybrid film through the exfoliation/restacking route can promote electrochemical oxidation process towards $N_2H_4{\cdot}H_2O$ effectively.

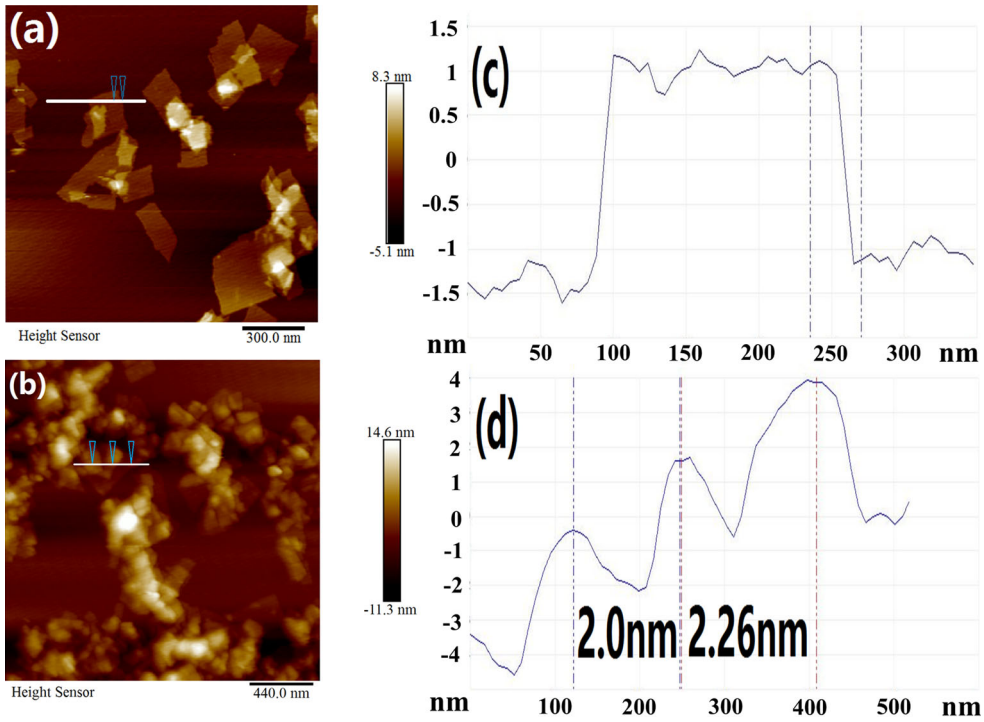

Figure 7 Typical AFM images of **a** $Sr_2Nb_3O_{10}^-$ nanosheets, **b** $Sr_2Nb_3O_{10}$/$CoTMPyP_1$ hybrid deposited on a mica substrate and **c**, **d** the corresponding section height profile along the marked white line.

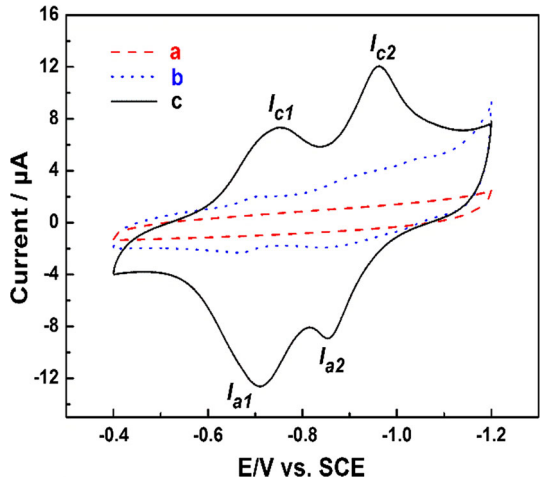

Figure 8 CV curves of (*a*) $KSr_2Nb_3O_{10}$ modified GCE (dash line), (*b*) CoTMPyP aqueous solution (dot line) and (*c*) $Sr_2Nb_3O_{10}$/$CoTMPyP_1$ modified GCE in N_2-saturated pH 12.0 B–R buffer solution at 100 mV s^{-1}.

Additionally, the influences of scan rate on CV behaviour of the final hybrid film were investigated in 0.2 M pH 7.0 PBS shown in (Fig. 9B). With the increase in the scan rate from 10 to 400 mV s^{-1}, the oxidation peak current increases gradually, and the oxidation peak potential moved towards negative, indicating the irreversibility of hydrazine hydrate oxidation process on $Sr_2Nb_3O_{10}$/$CoTMPyP_1$ modified GCE. According to the linear equation of I_{pa} (μA) = 6.11 + 61.15 $v^{1/2}$ ($V^{1/2}$ $s^{-1/2}$) (R = 0.9990) of the relationship curve plotted in the inset (Fig. 9B), a conclusion can be drawn that peak current (I_{pa}) was proportional to square root of the scan rate ($v^{1/2}$), demonstrating that electrochemical oxidation process on the surface of $Sr_2Nb_3O_{10}$/$CoTMPyP_1$ modified GCE was controlled by hydrazine hydrate diffusion. In addition, the inverted shape peaks were found in the CV curves of $Sr_2Nb_3O_{10}$/CoTMPyP towards hydrazine hydrate oxidation analogous to previous literatures [47, 48], which was probably ascribable to the formation of Co^{III}TMPyP–N_2H_4 complex in the electrochemical oxidation process, and thus, the possible mechanism of $N_2H_4{\cdot}H_2O$ oxidation that occurred on the modified electrode was proposed as follows referring to related literatures [49, 50]:

$$PCo^{III} + N_2H_4 \rightarrow PCo^{III}\cdots N_2H_4 \quad (1)$$

$$PCo^{III}\cdots N_2H_4 + 4H_2O \rightarrow PCo^{II} + N_2 + 4H_3O^+ + 3e^- \quad (2)$$

$$PCo^{II} - e^- \rightarrow PCo^{III} \quad (3)$$

P in the formula represents porphyrin ring, and the rate of the whole process is determined by the formation of Co^{III}TMPyP–N_2H_4 complex, namely the second step.

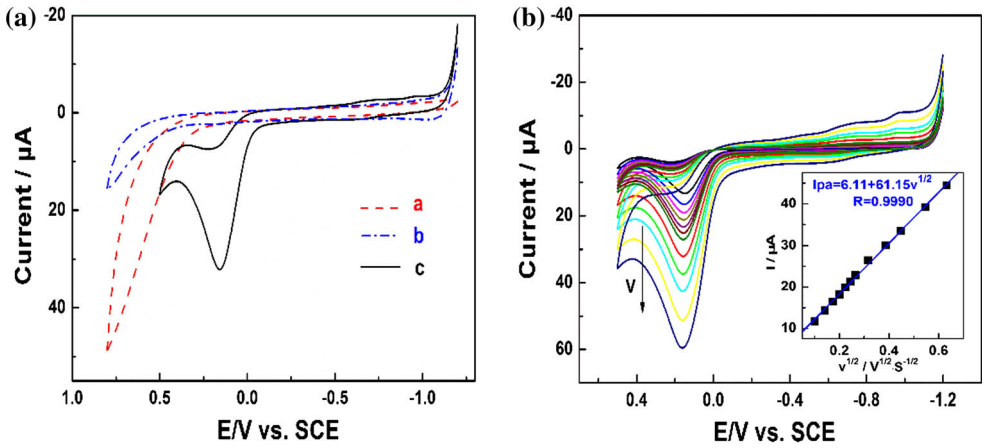

Figure 9 **A** CV curves of (*a*) bare GCE (dash line), (*b*) $KSr_2Nb_3O_{10}$ modified GCE (dash dot line), and (*c*) $Sr_2Nb_3O_{10}$/$CoTMPyP_1$ modified GCE (solid line) in N_2-saturated pH 7.0 PBS containing 3.92 mM $N_2H_4{\cdot}H_2O$ at 100 mV s^{-1}. **B** CV curves of $Sr_2Nb_3O_{10}$/$CoTMPyP_1$ modified GCE in N_2-saturated pH 7.0 PBS containing 3.92 mM $N_2H_4{\cdot}H_2O$ at 10, 20, 30, 40, 50, 60, 70, 100, 150, 200, 300, and 400 mV s^{-1}; the inset is the relationship curve between I_{pa} and $v^{1/2}$.

At last, the electrochemical determination of $N_2H_4{\cdot}H_2O$ using $Sr_2Nb_3O_{10}$/$CoTMPyP_1$ modified GCE was attempted with the peak current (I_{pa}) and hydrazine hydrate concentration (c) in hydrazine hydrate concentration of 0.05–0.99 mM in 0.2 M pH 7.0 PBS. As can be inferred from the relationship curve of the inset (Fig. 10), the peak current was proportional to hydrazine hydrate concentration with the calibration equation of I (μA) = 0.06 + 4.05c (mmol L^{-1}) (r = 0.9957); hence, a detection limit was calculated as 3.52 × 10^{-5} M at a signal-to-noise ratio of 3.0.

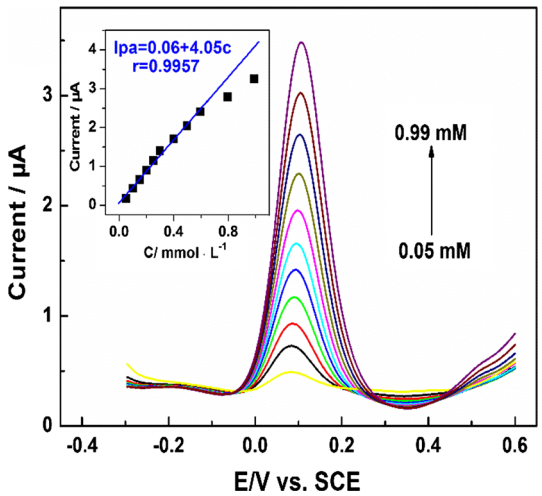

Figure 10 DPV curves of $Sr_2Nb_3O_{10}$/$CoTMPyP_1$ modified GCE in N_2-saturated pH 7.0 PBS solution with hydrazine hydrate concentration ranging from 0.05 to 0.99 mM; the inset is the relationship curve between I_{pa} and c.

Conclusions

The successful introduction of functional metalloporphyrin molecules (CoTMPyP) in large volume into the interlayer of $KSr_2Nb_3O_{10}$ through the convenient exfoliation/restacking route for the first time, which was confirmed by XRD, FTIR, UV–Vis, SEM, TEM, AFM, and ICP. Comparing with the crystallographic thickness of the $Sr_2Nb_3O_{10}^-$ laminate (1.44 nm), the observed thickness of $Sr_2Nb_3O_{10}^-$ nanosheet (2.18 nm) was likely to be homogeneously unilamellar, and the basal spacing of $Sr_2Nb_3O_{10}$/$CoTMPyP_1$ nanocomposite was measured as 2.0, 2.26 nm (AFM) and 2.04 nm (TEM) corresponding well to XRD data (2.05 nm). Besides, the well-dispersed and stable $Sr_2Nb_3O_{10}^-$ nanosheets colloidal dispersion with the zeta potential value of − 44.2 mV was obtained, and the zeta potential value was close to 0 mV when the volume ratio of CoTMPyP aqueous solution to $Sr_2Nb_3O_{10}^-$ nanosheets colloidal dispersion was 0.22. The fabrication of $Sr_2Nb_3O_{10}^-$ and CoTMPyP cations through electrostatic self-assembly will facilitate the development of a variety of novel functional nanocomposites based on D–J-type perovskite nanosheets. Eventually, the final self-assembled hybrid film prepared by drop-coating method exhibited excellent electro-catalytic activities towards $N_2H_4{\cdot}H_2O$ oxidation in pH 7.0 PBS, which makes it a promising electro-catalyst towards $N_2H_4{\cdot}H_2O$ oxidation; meanwhile, this paper also provides theoretical

basis for oxidation of $N_2H_4{\cdot}H_2O$ by virtue of functional nanocomposites associated with metalloporphyrin complex. Finally, a detection limit was estimated as 3.52×10^{-5} M according to a signal-to-noise ratio of 3.0.

Acknowledgements

This work was supported by National Natural Science Foundation of China (Grant Nos. 21401062, 21201070, 51202079), Natural Science Fund of Jiangsu Province (BK20161294, BK20140447, BK20141247, SBK201220654), University Science Research Project of Jiangsu Province (13KJB430005, 12KJD150001, 15KJB430004), Key R&D Project of Jiangsu Province (CG1602, CG1622), HHIT Research Project (Z2015011, Z2014004), and 521 High-level Personnel Training Research Project of Lianyungang City (KK15041).

Electronic supplementary material: The online version of this article (https://doi.org/10.1007/s10853-018-2033-x) contains supplementary material, which is available to authorized users.

References

[1] Rosca V et al (2009) Nitrogen cycle electrocatalysis. Chem Rev 109:2209–2244

[2] Aldous L, Compton RG (2011) The mechanism of hydrazine electro-oxidation revealed by platinum microelectrodes: role of residual oxides. Phys Chem Chem Phys 13:5279–5287

[3] Serov A, Kwak C (2010) Direct hydrazine fuel cells: a review. Appl Catal B Environ 98:1–9

[4] Li Z, Han C, Shen J (2006) Reduction of Ni^{2+} by hydrazine in solution for the preparation of nickel nano-particles. J Mater Sci 41:3473–3480. https://doi.org/10.1007/s10853-005-5874-z

[5] Sanabria-Chinchilla J et al (2011) Noble metal-free hydrazine fuel cell catalysts: EPOC effect in competing chemical and electrochemical reaction pathways. J Am Chem Soc 133:5425–5431

[6] Asazawa K et al (2007) A platinum-free zero-carbon-emission easy fuelling direct hydrazine fuel cell for vehicles. Angew Chem Int Edit 46:8024–8027

[7] Kumar AVN, Joseph J (2014) New Zn–NiHCF hybrid electrochemically formed on glassy carbon: observation of thin layer diffusion during electro-oxidation of hydrazine. J Phys Chem C 119:296–304

[8] Yamazaki SI et al (2012) Electrochemical oxidation of hydrazine derivatives by carbon-supported metalloporphyrins. J Power Sources 204:79–84

[9] Geraldo D et al (2002) Volcano correlations between formal potential and Hammett parameters of substituted cobalt phthalocyanines and their activity for hydrazine electro-oxidation. Electrochem Commun 4:182–187

[10] Hosseini M, Momeni MM (2010) Silver nanoparticles dispersed in polyaniline matrixes coated on titanium substrate as a novel electrode for electro-oxidation of hydrazine. J Mater Sci 45:3304–3310. https://doi.org/10.1007/s10853-010-4347-1

[11] Biesaga M et al (2000) Porphyrins in analytical chemistry. A review. Talanta 51:209–224

[12] Goubert-Renaudin SN et al (2010) Synthesis and characterization of carbon-supported transition metal oxide nanoparticles—cobalt porphyrin as catalysts for electroreduction of oxygen in acids. Electrochem Commun 12:1457–1461

[13] Halma M et al (2008) Synthesis, characterization, and catalytic activity of anionic iron(III) porphyrins intercalated into layered double hydroxides. J Catal 257:233–243

[14] Allen MR et al (2009) Evolution of physical and photocatalytic properties in the layered titanates $A_2Ti_4O_9$ (A = K, H) and in nanosheets derived by chemical exfoliation. Chem Mater 22:1220–1228

[15] Omomo Y et al (2003) Redoxable nanosheet crystallites of MnO_2 derived via delamination of a layered manganese oxide. J Am Chem Soc 125:3568–3575

[16] Osada M, Sasaki T (2012) Two-dimensional dielectric nanosheets: novel nanoelectronics from nanocrystal building blocks. Adv Mater 24:210–228

[17] Ma R, Sasaki T (2010) Nanosheets of oxides and hydroxides: ultimate 2D charge-bearing functional crystallites. Adv Mater 22:5082–5104

[18] Yin S et al (2013) Effects of reaction parameters on solution combustion synthesis of lepidocrocite-like $K_{0.80}Ti_{1.733-}Li_{0.267}O_4$: phase formation and morphology evolution. J Mater Sci 48:1533–1542. https://doi.org/10.1007/s10853-012-6908-y

[19] Sasaki T, Watanabe M (1998) Osmotic swelling to exfoliation. Exceptionally high degrees of hydration of a layered titanate. J Am Chem Soc 120:4682–4689

[20] Maluangnont T et al (2013) Osmotic swelling of layered compounds as a route to producing high-quality two-dimensional materials. A comparative study of tetramethylammonium versus tetrabutylammonium cation in a lepidocrocite-type titanate. Chem Mater 25:3137–3146

[21] Sasaki T et al (2001) Layer-by-layer assembly of titania nanosheet/polycation composite films. Chem Mater 13:4661–4667

[22] Unal U et al (2003) Electrostatic self-assembly deposition of titanate(IV) layered oxides intercalated with transition metal complexes and their electrochemical properties. J Phys Chem B 107:12680–12689

[23] Ebina Y et al (2005) Photocatalyst of lamellar aggregates of RuO_x-loaded perovskite nanosheets for overall water splitting. J Phys Chem B 109:17212–17216

[24] Lin B et al (2013) Mesoporous cobalt-intercalated layered tantalotungstate with high visible-light photocatalytic activity. Microporous Mesoporous Mater 172:105–111

[25] Oshima T et al (2015) Intercalation of highly dispersed metal nanoclusters into a layered metal oxide for photocatalytic overall water splitting. Angew Chem Int Edit 54:2698–2702

[26] Gunjakar JL et al (2011) Mesoporous layer-by-layer ordered nanohybrids of layered double hydroxide and layered metal oxide: highly active visible light photocatalysts with improved chemical stability. J Am Chem Soc 133:14998–15007

[27] Li L et al (2007) Layer-by-layer assembly and spontaneous flocculation of oppositely charged oxide and hydroxide nanosheets into inorganic sandwich layered materials. J Am Chem Soc 129:8000–8007

[28] Pan B et al (2016) Research on the self-assembly of exfoliated perovskite nanosheets ($LaNb_2O_7^-$) and cobalt porphyrin utilized for the electrocatalytic oxidation of ascorbic acid. RSC Adv 6:46388–46393

[29] Ebina Y et al (2012) Synthesis and in situ X-ray diffraction characterization of two-dimensional perovskite-type oxide colloids with a controlled molecular thickness. Chem Mater 24:4201–4208

[30] Takagaki A et al (2003) Exfoliated nanosheets as a new strong solid acid catalyst. J Am Chem Soc 125:5479–5485

[31] Dion M et al (1981) Nouvelles familles de phases $M^IM^{II}_2Nb_3O_{10}$ a feuillets "perovskitesh". Mater Res Bull 16:1429–1435

[32] Sun L et al (2007) Preparation of exfoliated epoxy/α-zirconium phosphate nanocomposites containing high aspect ratio nanoplatelets. Chem Mater 19(7):1749–1754

[33] Yu J et al (2015) One-step direct synthesis of layered double hydroxide single-layer nanosheets. Nanoscale 7(21):9448–9451

[34] Liu Z et al (2006) Synthesis, anion exchange, and delamination of Co-Al layered double hydroxide: assembly of the exfoliated nanosheet/polyanion composite films and magneto-optical studies. J Am Chem Soc 128:4872–4880

[35] Park IY, Kuroda K, Kato C (1989) Preparation of a layered double hydroxide-porphyrin intercalation compound. Chem Lett 11:2057–2058

[36] Yao K et al (2003) Spectroscopic and photoelectrochemical study of sensitized layered niobate $K_4Nb_6O_{17}$. Langmuir 19:321–325

[37] Yao K et al (2001) Spectroscopic and photoelectrochemical differences between racemic and enantiomeric $[Ru(phen)_3]^{2+}$ ions intercalated into layered niobate $K_4Nb_6O_{17}$. J Electroanal Chem 510:144–148

[38] Unal U et al (2006) Visible light photoelectrochemical activity of $K_4Nb_6O_{17}$ intercalated with photoactive complexes by electrostatic self-assembly deposition. J Solid State Chem 179:33–40

[39] Ozawa TC et al (2007) Preparation and characterization of the Eu^{3+} doped perovskite nanosheet phosphor: $La_{0.90}Eu_{0.05}Nb_2O_7$. Chem Mater 19:6575–6580

[40] Ozawa TC et al (2008) A new nanosheet phosphor with the high intrananosheet site photoactivator concentration. J Phys Chem C 112:1312–1315

[41] Ida S et al (2006) Photoluminescence properties of multilayer oxide films intercalated with rare earth ions by the layer-by-layer technique. Chem Commun 34:3619–3621

[42] Zhai Z et al (2011) Thermostable nitrogen-doped $HTiNbO_5$ nanosheets with a high visible-light photocatalytic activity. Nano Research 4(7):635–647

[43] Zhai Z et al (2012) Novel mesoporous NiO/$HTiNbO_5$ nanohybrids with high visible-light photocatalytic activity and good biocompatibility. Nanoscale 4(2):547–556

[44] Zhai Z et al (2012) Nitrogen-doped mesoporous nanohybrids of TiO_2 nanoparticles and $HTiNbO_5$ nanosheets with a high visible-light photocatalytic activity and a good biocompatibility. J Mater Chem 22(36):19122–19131

[45] Liu C et al (2014) The nanocomposite of polyaniline and nitrogen-doped layered $HTiNbO_5$ with excellent visible-light photocatalytic performance. Phys Chem Chem Phys 16(26):13409–13417

[46] Chen SM et al (2001) The catalytic and photocatalytic autoxidation of S_x^{2-} to SO_4^{2-} by water-soluble cobalt porphyrin. J Mol Catal A: Chem 166(2):243–253

[47] Ardiles P et al (2001) Electrocataltyic oxidation of hydrazine at polymeric iron-tetraaminophthalocyanine modified electrodes. J Mol Catal A: Chem 165(1):169–175

[48] Green MP et al (1989) In situ scanning tunneling microscopy studies of the underpotential deposition of lead on gold (111). J Phys Chem 93(6):2181–2184

[49] Ozoemena KI, Nyokong T (2005) Electrocatalytic oxidation and detection of hydrazine at gold electrode modified with iron phthalocyanine complex linked to mercaptopyridine self-assembled monolayer. Talanta 67:162–168

[50] Muthukumar P, John SA (2014) Efficient oxidation of hydrazine using amine-functionalized cobalt and nickel porphyrin-modified electrodes. J Solid State Electrochem 18(9):2393–2400